Electronic Supplementary Material (ESI) for Nanoscale.

Mapping plasmonic topological states at nanoscale. Supplementary information

Ivan S. Sinev,[1] Ivan S. Mukhin,[1] Alexey P. Slobozhanyuk,[1,2] Alexander N. Poddubny,[1,3] Andrey E. Miroshnichenko,[2] Anton K. Samusev,[1] and Yuri S. Kivshar[1,2]

[1]*ITMO University, St. Petersburg 197101, Russia*

[2]*Nonlinear Physics Centre, Australian National University, Acton, ACT, 2601, Australia*

[3]*Ioffe Physical-Technical Institute, Russian Academy of Sciences, St. Petersburg 194021, Russia*

(Dated: May 21, 2015)

NUMERICAL SIMULATION OF NSOM MAPS

The main disadvantage of the models interpreting the NSOM signal in terms of *local* electromagnetic fields is their inablility to give account for the effects depending shape of NSOM probe, which often plays a crucial role in NSOM experiments. Here, in order to model the measured near-field signal we used two different approaches.

The first one is based on Lorentz's reciprocity theorem[1,2]. This model relates the fields picked up by the near-field probe to the fields that this probe emits when excited by a point (dipole) source placed at the position of the detector. Contrary to the local field models, it allows to take into account both the shape of the near-field probe and the non-locality of the detection process. Mathematically, the sensitivity of the NSOM detection system (often referred to as *mutual impedance*) to different components of the field is given by[1]

$$\mathbf{E}_{det} \cdot \mathbf{j}_{rec} = \int_S (\mathbf{E}_{exp} \times \mathbf{H}_{rec} - \mathbf{E}_{rec} \times \mathbf{H}_{exp}) \cdot d\mathbf{S}. \tag{1}$$

Here, $\mathbf{E}_{exp}$ and $\mathbf{H}_{exp}$ stand for the electric and magnetic fields near the investigated structure (*experimental* fields), which induce fields ($\mathbf{E}_{det}$) at the detector. In the meantime, $\mathbf{E}_{rec}$ and $\mathbf{H}_{rec}$ (*reciprocal* fields) are the fields emitted from the near-field probe when it is excited by a point dipole source $\mathbf{j}_{rec}$ placed at the position of the detector. Our NSOM system had no polarization differentiation, and therefore we assumed that the observed signal was proportional to the square of the electric field modulus at the detector position. Since the components of this field can be expressed from the mutual impedance calculated for two orthogonal dipole sources, $\mathbf{j}_{rec}$ and $\mathbf{j}_{rec}^{\perp}$, the signal intensity in our case was derived from the equation

$$I \propto |\mathbf{E}_{det} \cdot \mathbf{j}_{rec}|^2 + \left|\mathbf{E}_{det} \cdot \mathbf{j}_{rec}^{\perp}\right|^2. \tag{2}$$

To model the near-field signal patterns, we had to evaluate the equation (2) for each position of the tip with respect to disks. To simplify the calculations of the reciprocal fields on the chosen surface S, we exploited the similarity of the fields below the probe to the fields below a hole in a flat metal film[3]. Thus, we simulated the *reciprocal* fields below a 150 nm glass hole in a 300-nm thick aluminium film irradiated by either x- or y-oriented dipole placed in the far-field.

However, even this model cannot directly account for the interaction between the probe and the sample, which can play a decisive role in the formation of the near-field image of

plasmonic nanostructures[4]. The task of modelling the full "probe-sample" system for each position of the probe above the structure is unjustifiably complex. Therefore, to give some account for the influence of the probe on the near-field of the sample, we calculated the *experimental* field distribution near the zigzag chain under a perfectly conducting (PEC) layer introduced above the structure at a distance of 100 nm, corresponding to the distance to the probe during the scanning process. Such an approximation can be justified by the fact that the size of the probe tip is about a micron due to the aluminium layer thickness, that is about the size of the whole studied structure. The reason for choosing PEC over aluminium in the calculations was that a system with PEC layer required substantially less computational memory and time, while we found that their influence on the near fields of the sample was similar.

In Fig. S1b,c we illustrate the strong influence of the environment of the structure on the numerical maps of the near-field signal. The figure unambiguously demonstrates the difference between the near-field signal patterns calculated via reciprocity approach with and without the account for substrate and the near-field probe. The map reconstructed from the fields calculated for a structure in free space does not agree well enough with the experimental data. However, the second map, which is calculated with account for the substrate and the near-field probe in the approximation described above, shows better agreement with the experiment. In particular, it demonstrates the pronounced hotspots shifted with respect to the disks positions, which are also observed in the experimental near-field maps. The disks themselves appear dark in the reconstructed images in agreement with results of the near-field studies of plasmonic nanostructures reported elsewhere[4,5].

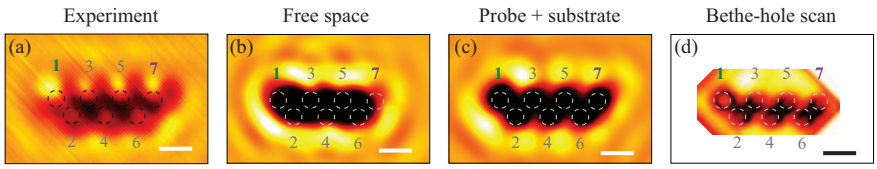

FIG. S1. Comparison of the experimental near-field pattern (a) and numerical near-field signal maps reconstructed from the field distributions for wavelength λ=700 nm calculated via reciprocity approach for a structure in free space (b) and with account for the substrate and the near-field probe influences (c) and by scanning a Bethe-hole analyzer over the structure (d). The regions far from the structure in panel (d) were not simulated due to heavy computation time requirements of the Bethe-hole scanning approach. Scale bars represent 500 nm.

As an alternative for reciprocity approach, we have also performed the simulation of NSOM signal for the resonant wavelength (700 nm) by scanning a Bethe-hole analyzer (150 nm hole in a PEC layer) over the zigzag structure with 50 nm step (see Fig. S1d). At each point, we calculated the signal transmitted through the hole into the far-field, which models the signal measured by a NSOM probe[6]. Fig. S1c reveals the differences of the near-field map as compared to the simulation for the PEC layer without a hole (Fig. S1c). In particular, the signal above the edge disk becomes more pronounced. However, the numerical map still does not exhibit one-to-one correspondence with the experimental results, indicating that the near-field signal measured in the experiment is influenced by other complex probe-sample interactions, e.g. excitation of surface plasmon polariton on the probe coating, multiple scattering etc., which are too difficult to be fully included in the simulations.

Since the Bethe-hole analyzer approach is extremely computation-heavy, to model the wavelength-dependent evolution of numerical NSOM maps we resorted to the approach based on reciprocity theorem with account for the substrate and the probe influences (Fig. S1c). Fig. S2 shows the comparison between the NSOM images of the studied structure reconstructed using this method and the experimental near-field maps for a set of different wavelengths. The rectangle highlights the results for the wavelength $\lambda = 700$ nm, where the contrast between the intensities of the signal from the edge disk and central disks is the strongest, as illustrated in Fig. 3c,d in the main text. The numerical maps demonstrate qualitative agreement with experimental data. The observed discrepancies can be attributed to the inaccuracy of modelling the near-field probe with a homogeneous conducting layer discussed above. However, the spectral dependence of the relative intensity of the hotspots observed near the edge disk (the plot is presented in Fig. 4c in the main text) demonstrates that the reconstructed patterns can also be used to characterize the excitation of the edge state.

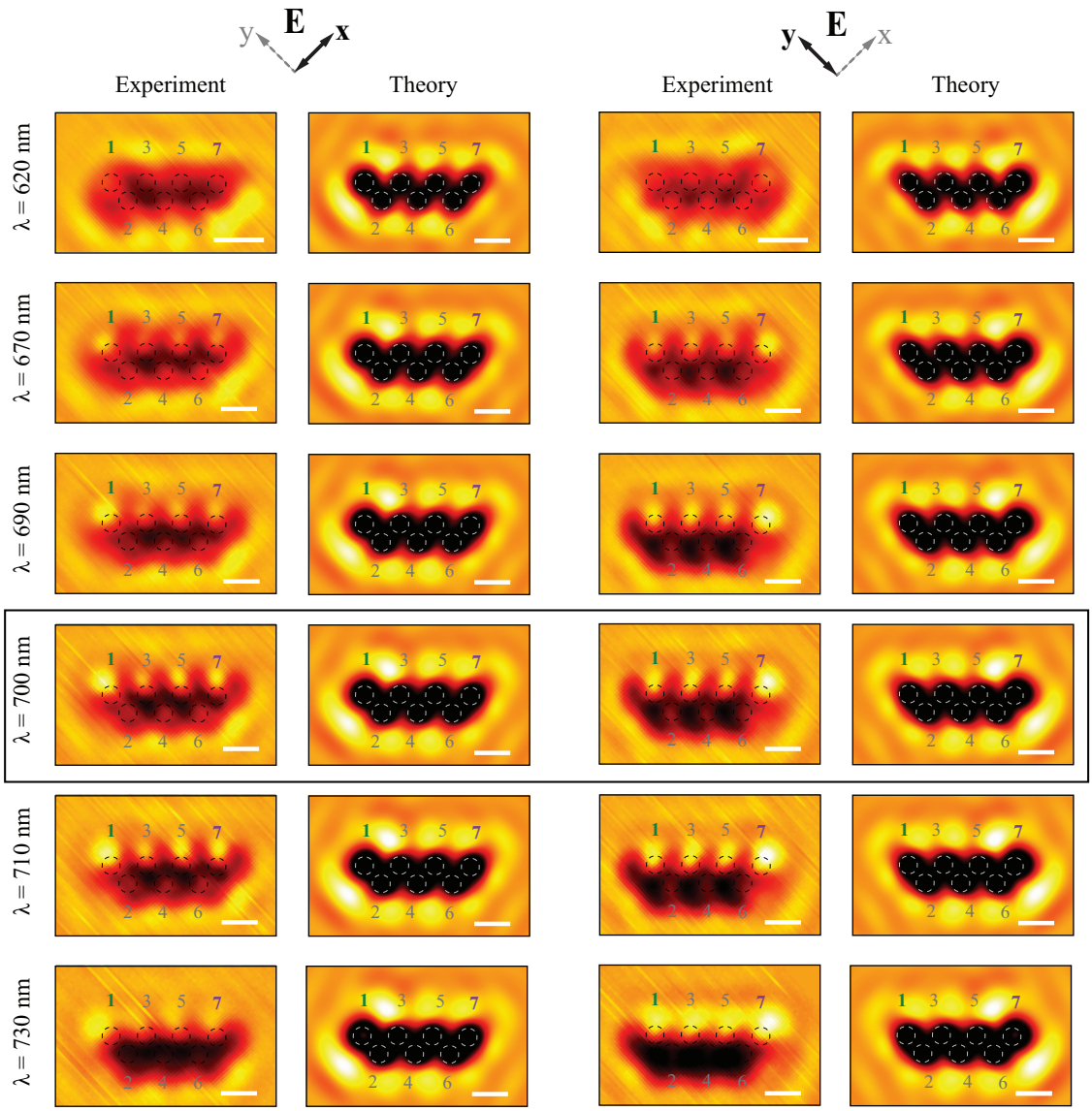

FIG. S2. Spectral dependence of the NSOM maps obtained from a zigzag chain of gold nanodisks for both x- and $y-$ polarizations compared with numerical NSOM signal reconstruction. Scale bars represent 500 nm.

PLASMONIC RESONANCES OF A SINGLE NANODISK

To analyze the optical response of a single gold nanodisk, we perform multipole decomposition of the scattered field in the vector spherical harmonics[7,8]. Fig. S3 presents the results of the multipole decomposition for the normal and in-plane incident directions, with the electric field along the diameter in both cases. For the normal incidence, only the electric dipole is excited at $\lambda \approx 800$ nm [see Fig. S3(a)], while for the in-plane excitation, the electric quadrupole is being resonantly excited as well at $\lambda \approx 600$ nm [see Fig. S3(b)].

Both considered dipole and quadrupole resonances are degenerate over polarization. For spherical particle the total polarization degeneracy of the multipole resonance is equal to $2L + 1$, where L is the angular momentum; $L = 1$ for the dipole mode and $L = 2$ for the quadrupole mode. In the case of disk the symmetry is reduced and the resonance is split. The resulting dipole and quadrupole eigenmodes of the disk are characterized by the absolute value of the angular momentum projection to the disk axis $|m|$. In particular, the considered dipole resonance corresponds to the two modes with the momentum projection $m = \pm 1$. The quadrupole resonance at $\lambda \approx 600$ nm corresponds to the two modes with $m = \pm 2$. It is more convenient to introduce the linear combinations of these modes as

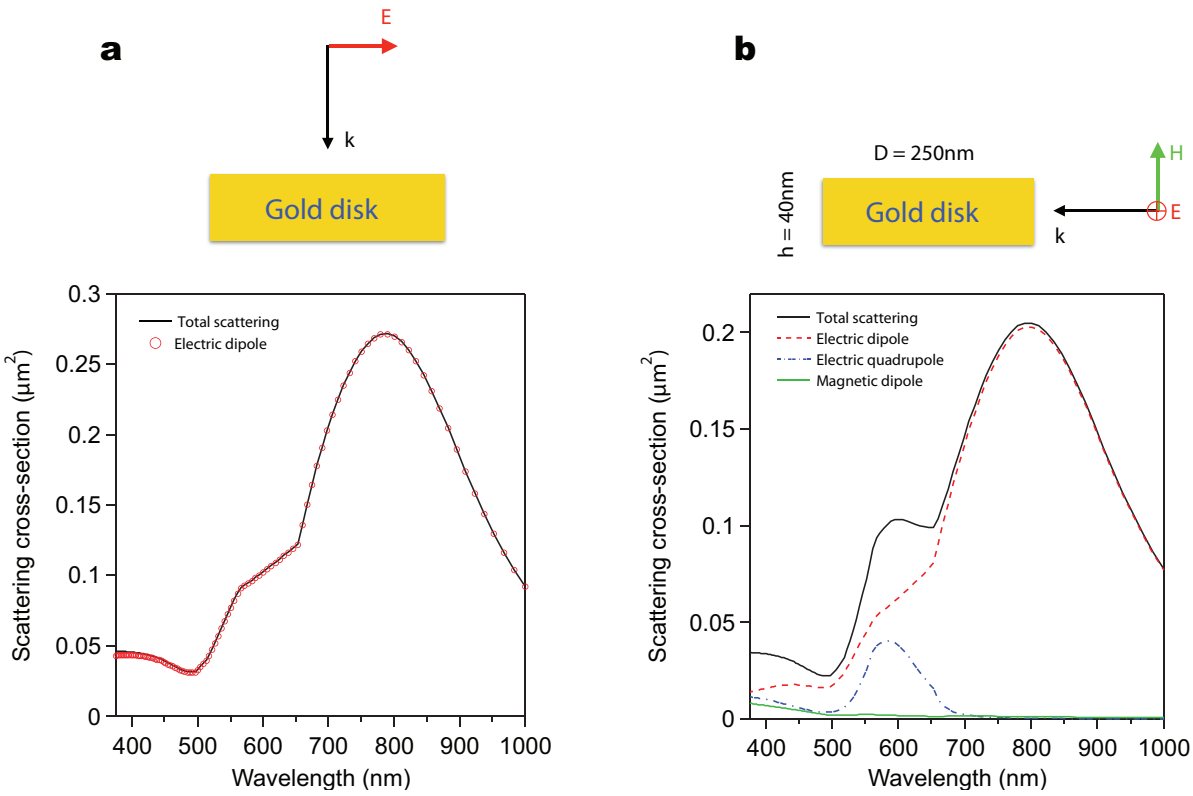

FIG. S3. Multipole decomposition of the scattered field from a single gold nanodisk for (a) normal and (b) in-plane excitations. Parameters of the gold nanodisk: diameter $D = 250$ nm and height $h = 40$ nm in free space. Along with the total scattering cross section (black), both electric dipole (red) and electric quadrupole (blue) contributions are shown.

follows:

$$p_x = \frac{p_1 - p_{-1}}{\sqrt{2}}\,, \quad p_y = \mathrm{i}\frac{p_1 + p_{-1}}{\sqrt{2}}\,, \tag{3}$$

for the dipole resonance and

$$Q_{xy} = \frac{Q_2 + Q_{-2}}{\sqrt{2}}\,, \quad Q_{x^2-y^2} = \frac{Q_2 - Q_{-2}}{\sqrt{2}\mathrm{i}} \tag{4}$$

for the quadrupole one. The dipole and quadrupole momenta can be expressed via the charge density ρ [9]:

$$p_x = \int d^3\boldsymbol{r} x\rho(\boldsymbol{r}), \qquad p_y = \int d^3\boldsymbol{r} y\rho(\boldsymbol{r}), \tag{5}$$

$$Q_{xy} = \int d^3\boldsymbol{r} xy\rho(\boldsymbol{r}), \qquad Q_{x^2-y^2} = \frac{1}{2}\int d^3\boldsymbol{r}(x^2-y^2)\rho(\boldsymbol{r})\,. \tag{6}$$

Next, we analyze the coupling between the dipole and quadrupole modes in the considered geometry. While the general theory including the retardation effects is available[10], here, for the sake of simplicity, we retain to the electrostatic near-field approximation that already captures the symmetry of the coupling. In particular, the multipole expansion of the potential including only the modes Eq. (5),Eq. (6) assumes the form

$$\varphi(\boldsymbol{r}) = -p_x\frac{\partial}{\partial x}\frac{1}{|\boldsymbol{r}-\boldsymbol{R}|} - p_y\frac{\partial}{\partial y}\frac{1}{|\boldsymbol{r}-\boldsymbol{R}|} + \frac{1}{2}Q_{xy}\frac{\partial^2}{\partial x\partial y}\frac{1}{|\boldsymbol{r}-\boldsymbol{R}|} + \frac{1}{2}Q_{x^2-y^2}\left(\frac{\partial^2}{\partial x^2} - \frac{\partial^2}{\partial y^2}\right)\frac{1}{|\boldsymbol{r}-\boldsymbol{R}|}\,. \tag{7}$$

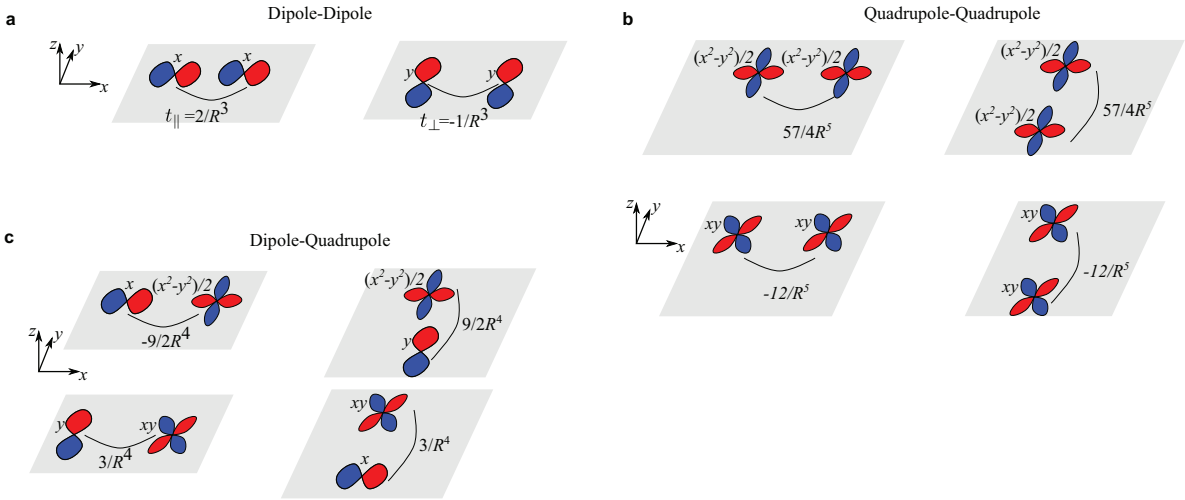

FIG. S4. Coupling constants for the dipole-dipole (a), quadrupole-quadrupole (b) and dipole-quadrupole (c) interaction. The definition of the eigenmodes corresponds to Eq. (3) and Eq. (4), R is the distance between the disk centers.

Here, $\boldsymbol{R}$ is the radius-vector of the disk center, specifying the origin of the multipole expansion. In order to obtain the coupling constants, describing the interaction between the multipoles, centered in the points $\boldsymbol{r} = 0$ and $\boldsymbol{r} = \boldsymbol{R}$, one has to calculate the derivatives of the potential Eq. (7) at the point $\boldsymbol{r} = 0$. The dipole mode respond to the electric field $\boldsymbol{E} = -\nabla\varphi$ at $\boldsymbol{r} = 0$,

$$p_x \propto E_x, \quad p_y \propto E_y \tag{8}$$

and the quadrupole modes probe the derivatives of the electric field,

$$Q'_{xy} \propto \frac{1}{2}\left(\frac{\partial E_x}{\partial y} + \frac{\partial E_y}{\partial x}\right), \quad Q'_{x^2-y^2} \propto \frac{1}{4}\left(\frac{\partial E_x}{\partial x} - \frac{\partial E_y}{\partial y}\right). \tag{9}$$

The resulting coupling constants are summarized in Fig. S4. Different panels correspond to two possible orientations of the vector $\boldsymbol{R}$ between the nearest neighbors in the zigzag geometry (along x and along y) and to different combinations of the multipole momenta.

The dipole-dipole coupling is described by the two constants, $t_{\parallel} = 2/R^3$ and $t_{\perp} = -1/R^3$, corresponding to the dipole momenta oriented along and perpendicular to the axis between the disks. As discussed in the main text of the paper, this coupling leads to the Su-Schrieffer-Heeger model independently for x- and y- polarized coupled modes of the disks in the zigzag chain.

The quadrupole-quadrupole coupling [see Fig. S4b] is the same for the pair of the disks oriented along x and along y directions. This coupling also does not mix $x^2 - y^2$ and xy modes. Thus, the symmetry of the interaction is very different from the case of the dipole modes and reflects higher rotational symmetry of the quadrupole modes: their spatial distribution is not changed under the rotation by $\pi/2$. Hence, the quadrupole modes have qualitatively the same coupling for the zigzag chain and for the linear chain. It is not possible to realize the edge states in the zigzag chain with the bond angle equal to $\pi/2$ that are based only on the quadrupole-quadrupole coupling.

The symmetry also allows the coupling between the dipole and quadrupole modes (Fig. S4c). This coupling is sensitive to the mutual orientation of the modes and is different for zigzag and linear chains. The dipole-quadrupole coupling, in turn, induces effective polarization-dependent coupling between the quadrupole modes. It can be shown, that in the finite chain such coupling leads to the two polarization-degenerate edge states at the quadrupole resonance. Hence, the structure can manifest polarization-degenerate edge states both at the dipole and at the quadrupole resonances. In the actual experimental

system the dipole and the quadrupole resonances are spectrally overlapping due to the radiation and Ohmic losses (Fig. 3 in the main text).

---

[1] J.A. Porto, R. Carminati, and J.-J. Greffet, "Theory of electromagnetic field imaging and spectroscopy in scanning near-field optical microscopy," J. Appl. Phys. **88**, 4845 (2000)

[2] I. Sinev, P. Voroshilov, I. Mukhin, A. Denisyuk, M. Guzhva, A. Samusev, P. Belov, and C. Simovski, "Demonstration of unusual nanoantenna array modes through direct reconstruction of the near-field signal," Nanoscale **7**, 765 (2015)

[3] B. le Feber, N. Rotenberg, D.M. Beggs, and L. Kuipers, "Simultaneous measurement of nanoscale electric and magnetic optical fields," Nat. Photon. **8**, 43 (2014)

[4] D. Denkova, N. Verellen, A. Silhanek, P. Van Dorpe, and V. Moshchalkov, "Lateral Magnetic Near-Field Imaging of Plasmonic Nanoantennas With Increasing Complexity," Small **10**, 1959 (2014)

[5] H. Okamoto, and K. Imura, "Visualizing the Optical Field Structures in Metal Nanostructures," J. Phys. Chem. Lett. **4**, 2230 (2013)

[6] D. Denkova, N. Verellen, A. Silhanek, P. Van Dorpe, and V. Moshchalkov, "Near-field aperture-probe as a magnetic dipole source and optical magnetic field detector," arXiv:1406.7827v1

[7] J.D. Jackson, *Classical Electrodynamics, 3rd ed* (Wiley, 1998)

[8] P Grahn, A Shevchenko, and M Kaivola, "Electromagnetic multipole theory for optical nanomaterials," New J. Phys. **14**, 093033 (2012)

[9] L.D. Landau and E.M. Lifshitz, *Electrodynamics of Continuous Media* (Pergamon, New York, 1974)

[10] A.B. Evlyukhin, C. Reinhardt, U. Zywietz, and B.N. Chichkov, "Collective resonances in metal nanoparticle arrays with dipole-quadrupole interactions," Phys. Rev. B **85**, 245411 (2012)